# Measurements of scalar power spectra in high Schmidt number turbulent jets

Paul L. Miller and Paul E. Dimotakis

*Graduate Aeronautical Laboratories*
*California Institute of Technology*
*Pasadena, California 91125*

**Abstract**

Single-point, jet-fluid concentration measurements obtained from high Schmidt number ($Sc \simeq 1.9 \times 10^3$) turbulent jets permit an investigation of temporal scalar power spectra, for jet Reynolds numbers in the range of $1.25 \leq Re \times 10^{-4} \leq 7.2$. At intermediate scales, we find a spectrum with a logarithmic derivative (slope) that is increasing with Reynolds number, in absolute value, but less than $5/3$ at the highest Reynolds number in our experiments. At the smallest scales, our spectra exhibit no $k^{-1}$ power-law behavior, possessing a log-normal region over a range of scales exceeding a factor of 40, in some cases.

9 November 1992

## 1. Introduction

We report here on an experimental investigation of temporal scalar power spectra of round, high Schmidt number, turbulent jets. It is part of a larger effort to better understand mixing in turbulent free shear flows, including jets and shear layers. In these experiments, we examined the jet fluid concentration (scalar) power spectra for several reasons. Spectra are sensitive diagnostics of the flow, providing information over a wide range of scales. Historically, they have been the object of a great deal of attention, partially because it is possible to extract predictions for spectral slopes from various turbulence theories and models.

Key among these turbulence theories are the 1941 paper by Kolmogorov,[1] with implications for the scalar field in the inertial range discussed by Corrsin,[2] Oboukhov,[3] and, for higher wavenumbers, the theory by Batchelor.[4] See, for example, discussions in Monin and Yaglom,[5] as well as in the recent review by Gibson.[6] Both the Corrsin and the Oboukhov theories yield predictions of power-law spectra and of the spectral power-law logarithmic derivative, or *slope*, as it will be subsequently referred to in this paper. Specifically, the Corrsin and Oboukhov theories predict a scalar spectrum proportional to $k^{-5/3}$ in the inertial range, as did the 1941 Kolmogorov theory for the energy spectrum.

For energy spectra, this has been observed experimentally under many conditions (*cf.* compilation of data by Chapman[7]). The situation is less clear concerning scalar spectra, with departures from the predicted behavior continuing to fuel debate about details and refinements of the theory.

Batchelor[4] and Batchelor *et al.*[8] recognized that for Schmidt, or Prandtl, numbers away from unity there exists an additional, scalar-diffusion, scale, now commonly referred to as the *Batchelor scale*, which admits a change in the scalar spectral behavior. The Batchelor theory[4] predicted that the scalar power spectrum at high Schmidt numbers would display a $k^{-1}$ dependence beyond the Kolmogorov wavenumber, *i.e.*, a spectral slope of $-1$. Measurements in the laboratory (*e.g.*, Gibson and Schwarz[9]) and the ocean (*e.g.*, Grant *et al.*[10]) were subsequently reported to be in accord with this prediction.

On the other hand, more recent measurements by Gargett[11] in the ocean were found not to exhibit a $k^{-1}$ spectral range (see, however, discussion by Gibson in Refs. 12 and 6). The same result was noted in passive scalar mixing measurements in shear layers[13] and in scalar measurements in turbulent jets.[14,15] Specifically, despite adequate resolution in those experiments, no $k^{-1}$ range was found at high spatial wavenumbers, or, to be exact, temporal frequencies, adding to the questions about the universality, if not the validity,[16] of the classical predictions at high Schmidt number.

The issue of spatial, *vs.* temporal, spectra should be recognized here. The classical theories cited deal with spatial spectra. One could argue, therefore, that comparisons of measurements of temporal spectra with predictions of spatial spectra cannot be made directly. Two points, however, should be noted in response. First, the overwhelming majority of experimentally obtained spectra reported in accord with the theoretical predictions have, in fact, been temporal. Second, at least in the case of developing flows that are not (statistically) spatially homogeneous over the range of spectral scales of interest, the notion of a spatial spectrum and the assumption of a statistically spatially homogeneous turbulent field is questionable. Temporal spectra, derived from point measurements, do not have to contend with this issue.

## 2. Experiment

The experiments investigated the scalar (concentration) field of round, axisymmetric, momentum-dominated, turbulent jets issuing from contoured nozzles into a large, quiescent discharge tank. The measurements were performed in the far field, on the centerline of the jet. Details of the experimental apparatus have appeared previously,[14–17] so only a brief overview will be presented here.

The experimental facility consists of three major parts: the jet plenum, nozzle, and delivery system; a large reservoir that acts as the discharge tank; and the diagnostics, consisting of an argon-ion laser, focusing optics, collection optics, detector, signal-processing electronics, and the subsequent data-processing. The

working fluid is water, and the scalar is a laser dye (disodium fluorescein) which is homogeneously premixed with the jet plenum fluid. The resulting Schmidt number,

$$Sc \equiv \frac{\nu}{\mathcal{D}} \tag{1}$$

with $\nu$ the kinematic viscosity of water and $\mathcal{D} \simeq 5.2 \times 10^{-6}\,\mathrm{cm}^2/\mathrm{s}$ the estimated aqueous species diffusivity of the fluorescein dye (Ref. 18, p. 280), is $1.9 \times 10^3$.

The jet flow was established and maintained by pressurizing a downward oriented jet plenum with gas. Both sonically-metered and blow-down, nearly constant pressure, gas delivery configurations were used. The internal exit diameter of the jet nozzle is 2.5 mm (0.1 in.). The rectangular discharge tank is square in cross-section, approximately 2 m high and 1 m on edge. The tank bottom is over 600 nozzle diameters downstream. Large glass windows on all four sides provided optical access (see Ref. 15 for details).

The illumination source was an argon-ion laser (Coherent Innova 90). The particular unit was custom selected for its low AM noise figure ($\sim -95\,\mathrm{dB}$) over the frequency range of interest in these experiments. It was operated at a power of 3.5 W in the light-regulation mode. The beam was spatially filtered, expanded, collimated, and subsequently focused to a small waist located on the centerline of the jet. A low dye concentration was used in the jet plenum ($\sim 10^{-6}\,\mathrm{M}$), with correspondingly substantially lower concentrations at the measuring stations. A more detailed discussion of this and related issues may be found in Refs. 14 and 15. The emitted fluorescence intensity was then proportional to the local scalar (dye) concentration $c(\mathbf{x}, t)$, that was, in turn, averaged over the extent of the measurement volume.

The fluorescence emitted from the measurement volume was collected through a narrow slit spatial filter. The beam profile and the slit width defined a small, spatially-averaging volume, roughly spherical in shape and of extent (diameter) $\ell_a \approx 50\,\mu\mathrm{m}$, as estimated by direct observation using a cathetometer. We will return to this quantity later.

A photomultiplier tube (RCA 8645) was used to detect the fluorescence emitted from this volume. Its output signal was amplified by a custom-designed low-noise transimpedance amplifier, low-pass filtered using a third-order Butterworth filter, digitized, sampled with some margin with respect to the Nyquist frequency, and stored for subsequent processing.

The measurements to be discussed here were made in the far field, on the axis of the jet, for jet Reynolds numbers in the range of

$$1.25 \times 10^4 \leq Re \equiv \frac{u_0\, d}{\nu} \leq 7.2 \times 10^4 \ , \tag{2}$$

where $u_0$ is the nozzle exit velocity, $d$ the nozzle exit diameter, and $\nu$ is the kinematic viscosity. Data were also recorded at both lower and higher Reynolds numbers. The lower Reynolds number jets, however, behaved substantially differently, by any of a number of criteria, and were not accepted as representing *bona fide* turbulence.[14] In the other limit, the jet at the higher Reynolds number ($Re = 10.2 \times 10^4$) produced a distinct hissing sound. This was probably generated by the transient dilatation and subsequent oscillations of small air bubbles caused by the rapid reduction in pressure in such bubbles as they exited the nozzle, or by cavitation in the jet near-field region, or both (note that the plenum gauge pressure is quadratic with Reynolds number). See discussion and references in Ref. 19, pp. 452–453, and Ref. 20, pp. 205–207, for example. As a result, the $Re = 10.2 \times 10^4$ jet was exposed to different near-field conditions and will not be included in the discussion below. See Ref. 15 for a further documentation of the data.

Finally, constraints dictated by resolution and statistical convergence, *vis-à-vis* total number of large scale structures captured and length-of-run considerations, led to measurement stations in the range,

$$100 \leq \frac{x}{d} \leq 305 \ , \tag{3}$$

where $x$ is the distance from the nozzle exit.

## 3. Scalar power spectrum estimation

The fluorescence signal $\phi(t)$, representing the photon flux incident on the photodetector, is a linear function of the spatial average of the convected local jet-fluid concentration $c(\mathbf{x}, t)$ over the measurement volume. It produces a signal that can be approximated by a convolution over $c(t) = c(\mathbf{x}_0, t)$, the jet fluid concentration at, say, the center of the measurement volume, $\mathbf{x}_0$, *i.e.*,

$$\phi(t) \simeq \int_{-\infty}^{\infty} h_a(t - t')\, c(t')\, \mathrm{d}t' \equiv h_a(t) \otimes c(t) \ . \tag{4}$$

In this expression, $h_a(t)$ models the impulse response of the spatio-temporal averaging process, *i.e.*, the temporal signal that would be measured if a spatial delta function of dye was convected through the measurement volume at the local flow velocity. See Fig. 1.

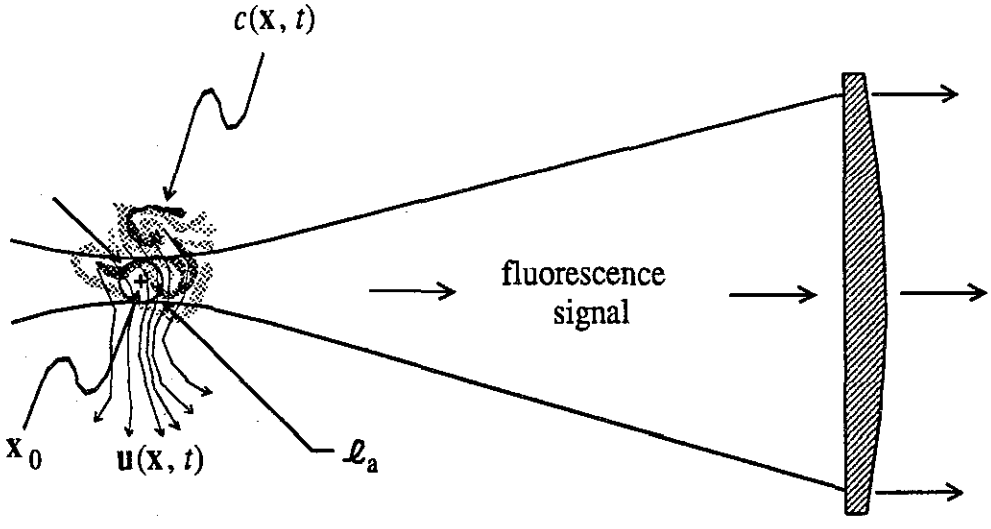


FIG. 1 Sketch of jet fluid concentration field $c(\mathbf{x}, t)$, convected through the measurement volume of extent $\ell_a$.

The fluorescence output $\phi(t)$, along with fluctuations contributed by the small laser intensity fluctuations, convected residual non-uniformities in the jet plenum dye concentration, photon shot noise, electronic noise generated by the signal-processing chain, *etc.*, was processed by the Butterworth low-pass filter to produce the total signal

$$s(t) = h_{\mathrm{LP}}(t) \otimes \phi(t) + n(t) = h(t) \otimes c(t) + n(t) \ , \tag{5}$$

that was digitized and stored. In this expression, $h(t) \equiv h_{\rm LP}(t) \otimes h_{\rm a}(t)$ is the total system transfer function and $n(t)$ is the total, low-pass-filtered noise.

Assuming that the total system noise $n(t)$ can be modeled as uncorrelated with the local dye concentration time history $c(t)$, the spectrum $S_s(\omega)$ of $s(t)$ can be expressed in terms of the spectrum $S_\phi(\omega)$ of $\phi(t)$ and the spectrum $S_n(\omega)$ of the (low-pass filtered) noise $n(t)$, *i.e.*,

$$S_s(\omega) \simeq S_\phi(\omega) + S_n(\omega) , \tag{6}$$

where, from Eq. 4,

$$S_\phi(\omega) \simeq |H_{\rm a}(\omega)|^2 S_c(\omega) , \tag{7}$$

with $H_{\rm a}(\omega) \equiv \mathcal{FT}\{ h_{\rm a}(t) \}$, the Fourier transform of $h_{\rm a}(t)$. This allows us to relate the total signal spectrum, $S_s(\omega)$, to the desired scalar fluctuation spectrum, $S_c(\omega)$, of $c(t)$, *i.e.*

$$S_s(\omega) \simeq |H(\omega)|^2 S_c(\omega) + S_n(\omega) \simeq |H_{\rm a}(\omega)|^2 S_c(\omega) + S_n(\omega) , \tag{8}$$

where $H(\omega) \equiv \mathcal{FT}\{ h(t) \} = H_{\rm LP}(\omega) H_{\rm a}(\omega)$.

For these experiments, the knee of the Butterworth low-pass filter was set substantially higher than the range of frequencies contained in $S_\phi(\omega)$. Its main purpose was to bandlimit the noise and de-alias the digitized measurements, allowing the noise-floor to be determined, as will be illustrated in the spectra presented below. This is the reason the modulus squared of $H_{\rm LP}(\omega)$, the transfer function of the low-pass filter, can be ignored in Eqs. 7 and 8, and wherever it multiplies $S_\phi(\omega)$ and $S_c(\omega)$.

Figure 2 illustrates these relations by comparing the spectrum $S_s(\omega)$ of the total signal s(t), *i.e.*, fluorescence $\phi(t)$ plus noise $n(t)$, with $S_\phi(\omega)$, the spectrum of the fluorescence signal alone. The latter was calculated by subtracting the estimated noise spectrum, $S_n(\omega)$, from the total spectrum $S_s(\omega)$. Recalling Eq. 6, we have

$$S_\phi(\omega) \simeq S_s(\omega) - S_n(\omega) . \tag{9}$$

The noise spectrum was assumed to be white, as was found to be the case in separate measurements of this quantity (see also Ref. 21 for examples). Nevertheless, the result is not sensitive to the assumed shape of the noise spectrum at low frequencies where $S_\phi(\omega)$ dominates. The data processed to produce the spectra in Fig. 2 were recorded at $x/d = 100$, for $Re = 1.25 \times 10^4$. Note the high dynamic range of the total signal spectrum, *i.e.*, the (logarithmic) difference of the low-frequency power to noise-floor power. Note also that the span to one-half the (scaled) sampling frequency is well beyond the noise-cross-over frequency. As can be seen, the frequency extent of the noise floor was substantial.

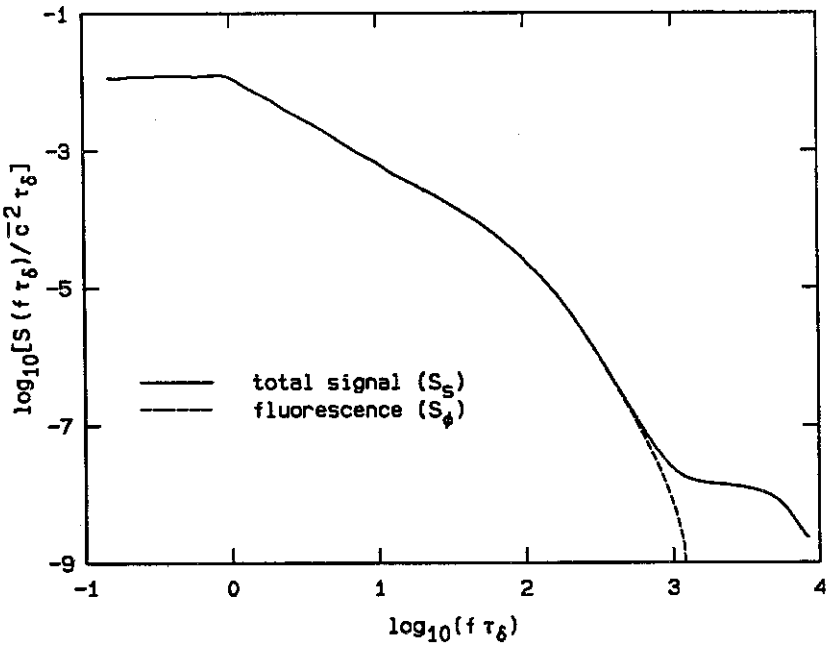


FIG. 2 Sample spectrum of the total signal (solid line: fluorescence + noise) and estimated fluorescence spectrum (dashed line: fluorescence), derived from measurements at $x/d = 100$, $Re = 1.25 \times 10^4$. Frequency scaled by $\tau_\delta(x)$, the local large-scale-passage time.

The spectra in Fig. 2, and throughout this paper, are normalized by $\overline{c}^2$, the square of the local mean value of $c(t)$, multiplied by the local large-scale-passage time, $\tau_\delta(x)$, and plotted in terms of the circular frequency, $f$, scaled by $\tau_\delta(x)$. In these coordinates, their integral produces the normalized variance, *e.g.*,

$$\frac{c'^2}{\overline{c}^2} = \int_0^\infty \left[\frac{S_c(f\tau_\delta)}{\overline{c}^2\,\tau_\delta}\right] \mathrm{d}f\tau_\delta \ . \tag{10}$$

The local large-scale-passage time, $\tau_\delta$, is given by,

$$\tau_\delta(x) \equiv \frac{\delta(x)}{u_{\rm cl}(x)} \ , \tag{11a}$$

where

$$\delta(x) \simeq 0.41\, x \ , \tag{11b}$$

is the local outer scale of the flow, here identified with the (measured) mean transverse extent (visual width) of the conical region enveloping the jet-fluid (Ref. 15, Appendix D), and $u_{\rm cl}(x)$ is the mean centerline velocity. The latter was estimated from the relation

$$\frac{u_{\rm cl}(x)}{u_{\rm j}} = 6.2\, \frac{d}{x - x_{\rm j}} \ , \tag{11c}$$

where $u_{\rm j}$ is the jet velocity and $x_{\rm j}$ the jet (virtual) origin, recommended by Chen and Rodi.[22] This spectrum and frequency scaling was found to produce similarity with respect to the downstream coordinate, $x/d$, in the analysis of scalar spectra measured in gas-phase jets.[23]

The spectrum $S_c(\omega)$ of the scalar fluctuations $c(t)$ can, at least formally, be estimated by solving Eq. 7, *i.e.*,

$$S_c(\omega) \simeq \frac{S_\phi(\omega)}{|H_{\rm a}(\omega)|^2} \ , \tag{12a}$$

or Eq. 8, yielding a result in terms of experimentally estimated quantities, *i.e.*,

$$S_c(\omega) \simeq \frac{S_s(\omega) - S_n(\omega)}{|H_{\rm a}(\omega)|^2} \ . \tag{12b}$$

We should note, at this point, that Eq. 4, assuming a fixed $h_{\rm a}(t)$, is not a proper equation for two reasons. First, the fluid velocity convecting the $c(\mathbf{x}, t)$-field through the measurement volume is not a constant. Second, different scalar field lagrangian trajectories through the measurement volume sample chords of different sizes (and transit times) through it. These two effects could, in principle, be expressed as two additional convolutions over the local velocity field and scalar paths through the measurement volume. See Fig. 1.

For frequencies, however, corresponding to spatial scales of the order of, or less than, the extent of the measurement volume, $\ell_a$, where the $H_a(\omega)$ transfer function will have an effect on the measurement of the scalar spectrum, fractional fluctuations in the convecting velocity are considerably smaller than fractional fluctuations in $c(\mathbf{x},t)$, at least for this high-Schmidt-number fluid. They are also, largely, uncorrelated with them. Fluid paths through the measurement volume are also uncorrelated with the passively-convected scalar field. As a consequence, in estimating the spectrum in the frequency neighborhood of

$$f\tau_\delta(x) \approx \frac{\delta(x)}{2\pi\,\ell_a} , \tag{13}$$

and above, these two effects do not contribute.

Alternatively, the most general expression of the linear dependence of the fluorescence signal, $\phi(t)$, on the local jet-fluid concentration, $c(t)$, is given by Eq. 7. While Eq. 7 follows from Eq. 4, the converse is not true. Equation 4 is more restrictive, also requiring a definite phase relation between $c(t)$ and $\phi(t)$. Fortunately, these (unknown) phase relations do not enter in the relation between the corresponding spectra. We may conclude that Eqs. 7 and 12 represent valid relations for the corresponding spectra, even as Eq. 4 cannot be accepted as a correct description of the time-history of the fluorescence signal $\phi(t)$.

The estimation of the scalar spectrum $S_c(\omega)$ in the frequency range influenced by the spatio-temporal averaging of the measurement process also requires knowledge of the $H_a(\omega)$ transfer function. This can be estimated, in turn, by noting that it is dominated by a pole corresponding to the transit time of the flow through the measurement volume, *i.e.*,

$$H_a(\omega) \sim \frac{1}{1 + i\,\omega\,\tau_a} , \tag{14a}$$

with

$$\tau_a \approx \frac{\ell_a}{u_{cl}(x)} . \tag{14b}$$

Performing two different experiments, under as identical flow conditions as was feasible, at two different spatial resolutions, we were able to compare the spectra, for $p = 1, 2$,

$$S_{s_p}(\omega) \simeq |H_p(\omega)|^2\, S_c(\omega) + S_{n_p}(\omega) , \tag{15a}$$

corresponding to two different locations of the dominant pole, at, say, $\tau_a = \tau_1$ and $\tau_a = \tau_2 > \tau_1$, *i.e.*, for $p = 1, 2$,

$$H_p(\omega) \simeq \frac{1}{1 + i\omega\tau_p} . \tag{15b}$$

If the scalar spectrum, $S_c(\omega)$, could be assumed to be identical in the two experiments (the corresponding noise floors were determined separately in each case), we see that the ratio of the two fluorescence spectra,

$$\frac{S_{\phi_1}}{S_{\phi_2}} \simeq \frac{S_{s_1}(\omega) - S_{n_1}(\omega)}{S_{s_2}(\omega) - S_{n_2}(\omega)} \equiv G(\omega; \tau_1, \tau_2) , \tag{16a}$$

would be given by

$$G(\omega; \tau_1, \tau_2) \simeq \frac{1 + (\omega\tau_2)^2}{1 + (\omega\tau_1)^2} = \begin{cases} 1 , & \text{for } \omega \ll 1/\tau_2 ; \\ (\tau_2/\tau_1)^2 , & \text{for } \omega \gg 1/\tau_1 , \end{cases} \tag{16b}$$

independently of the, as yet unknown, scalar spectrum, $S_c(\omega)$.

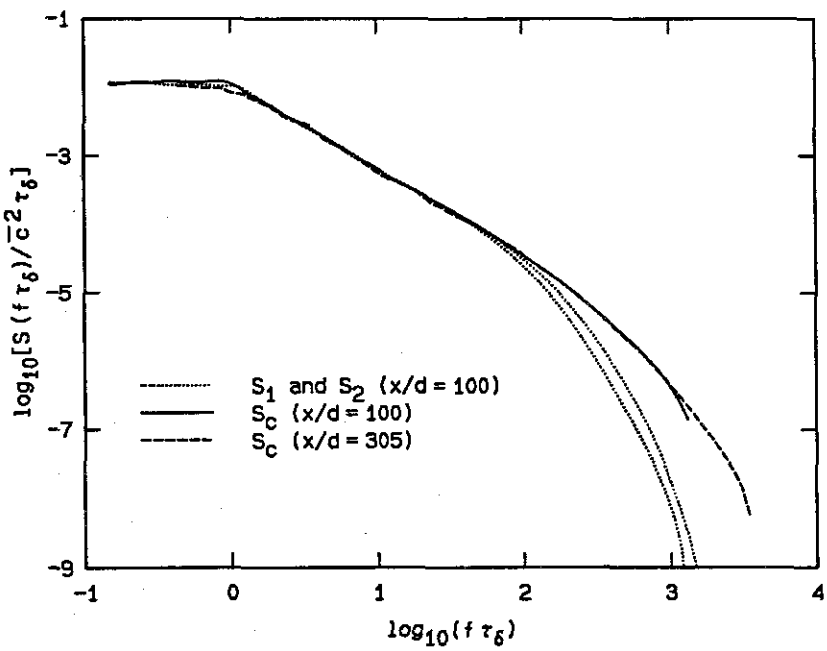


FIG. 3 Dotted lines: Fluorescence spectra estimated from measurements at $x/d = 100$ and $Re = 1.25 \times 10^4$ at two spatial resolutions. Solid line: Estimated concentration spectrum (Eq. 12) at $x/d = 100$ and $Re = 1.25 \times 10^4$. Dashed line: Estimated concentration spectrum at $x/d = 305$ and $Re = 1.2 \times 10^4$.

Two fluorescence spectra, $S_{\phi_1} = S_{s_1}(\omega) - S_{n_1}(\omega)$ and $S_{\phi_2} = S_{s_2}(\omega) - S_{n_2}(\omega)$, from one such pair of experiments, at $x/d = 100$ and $Re = 1.25 \times 10^4$, are plotted in Fig. 3 (dotted lines). The fluorescence spectrum with the larger high-frequency content is the one plotted in Fig. 2. Power spectra were computed numerically using a power spectral density estimation methodology that has evolved over the past ten years, or so. A documentation of some of its earlier features can be found in Ref. 24. In processing the data in the experiments reported here, the power spectral density estimation program computes spectra of data files by means of FFT methods, and incorporates Hanning windowing, contiguous record overlapping, and parabolic detrending, among other features. Records up to $2^{17}$ points can be accommodated. For spectra known to be smooth, the program can provide third-octave ($\simeq$ 1/10 decade) gaussian filtering, sampled at 20 points per decade, to produce the final spectra. This feature was used for all the spectra plotted in this paper, not so much for smoothing, but to reduce the number of points to a manageable level for plotting purposes (note that $2^{16} = 65{,}536$).

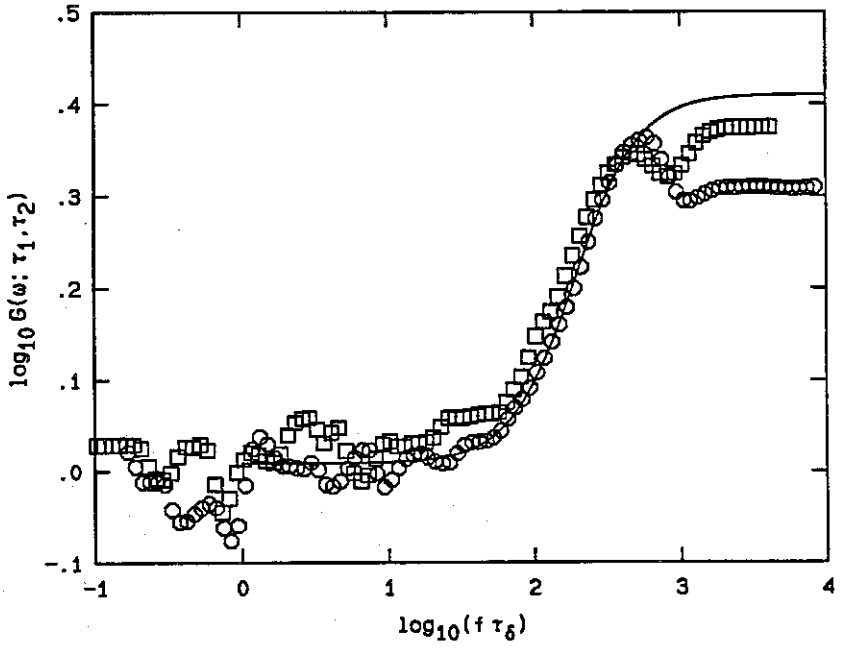


FIG. 4 Computed ratio, $G(\omega; \tau_1, \tau_2)$, of fluorescence spectra at $x/d = 100$ (Eq. 16). Circles: $Re = 1.25 \times 10^4$. Squares: $Re = 2.55 \times 10^4$. Solid line: Least squares fit for $\tau_1$ and $\tau_2$.

The ratios $G(\omega;\tau_1,\tau_2)$ for a pair of spectra, measured at $x/d = 100$, at $Re = 1.25\times10^4$ (circles) and a pair at $Re = 2.55\times10^4$ (squares), respectively, are plotted in Fig. 4. As can be seen, the ratios of spectra measured at different Reynolds numbers are very nearly the same, in accord with the analysis outlined above, even though, as we will see below, the spectra themselves are $Re$-dependent.

The curve (solid line) in Fig. 4 is a least-squares fit for $\tau_1$ and $\tau_2$ to the lower Reynolds number data, that were characterized by the higher signal-to-noise ratio, in the frequency range $1.0 \leq f\tau_\delta \leq 2.8$. The lower limit of the fit range is chosen so as to exclude (the small) run-to-run variations at frequencies well below those affected by the spatial averaging. The upper frequency limit is dictated by the less than unity signal-to-noise ratio at higher frequencies yet (*cf.* Fig. 2). The values for $\tau_1$ and $\tau_2$ estimated by this procedure were

$$2\pi\,\tau_1/\tau_\delta \simeq 4.2\times10^{-3} \qquad \text{and} \qquad 2\pi\,\tau_2/\tau_\delta \simeq 6.6\times10^{-3}\ , \tag{17}$$

respectively. This corresponds to an effective spatial extent of the measurement volume of $\ell_a \simeq 69\,\mu$m for the smaller of the two (Eq. 13), in reasonable accord with the visually estimated value of $\sim 50\,\mu$m using the cathetometer. This value was used to calculate the concentration spectrum, $S_c(\omega)$, at $x/d = 100$ and $Re = 1.25\times10^4$, plotted as the solid line in Fig. 3. It was computed from the fluorescence spectrum recorded at the higher resolution, using Eq. 12 with the estimated single-pole transfer function $H_a(\omega)$ of Eq. 14, at $\tau_a = \tau_1$.

The effective pole locations for data recorded at $x/d = 305$ were more difficult to estimate. At $x/d = 305$, the higher relative spatial resolution pushed the poles closer to the noise cross-over point. On the other hand, at $x/d = 305$, the (logarithmic) difference between the fluorescence and estimated concentration spectra was much smaller over the frequency range of interest. Figure 5 plots the fluorescence spectrum (dotted line) at $x/d = 305$ and $Re = 1.2\times10^4$ as well as the estimated concentration spectrum (dashed line). As can be seen, the effects of compensation, in this case, are much smaller (*cf.* difference at, say, $f\tau_\delta \simeq 2.7$ in Figs. 3 and 5). The estimated concentration spectrum at $x/d = 305$ in Fig. 5 is the one plotted as a dashed line in Fig. 3.

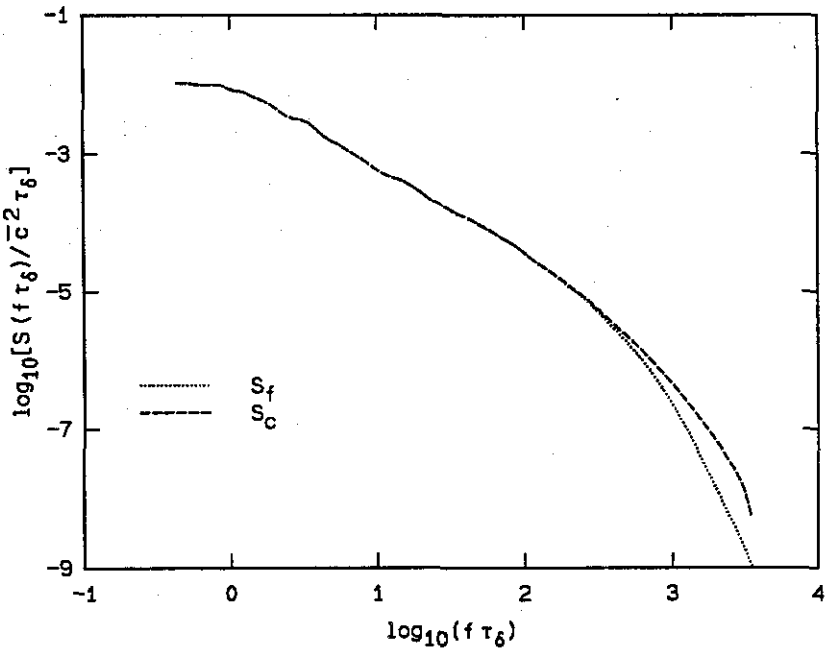


FIG. 5 Dotted line: Fluorescence spectrum. Dashed line: Estimated concentration spectrum. Data recorded at $x/d = 305$ and $Re = 1.2 \times 10^4$.

The jet fluid concentration spectra to be discussed below were all estimated in this fashion. The values of $\tau_a$, the transfer function time constant used in the compensation calculations, were fixed for all the data measured at each $x/d$ axial location (Eq. 17, for measurements at $x/d = 100$, depending on which slit width was used to record the fluorescence data). A fixed pair of values was also used for all the data measured at $x/d = 305$.

## 4. Results and discussion

The conspicuous agreement between the concentration spectra at $x/d = 100$ (solid line) and $x/d = 305$ (dashed line) in Fig. 3, up to frequencies limited by signal-to-noise ratio considerations, should be noted. A similar independence of the scaled spectra with downstream location was also found to hold in gas-phase jets,[23] where the relatively larger diffusion scales, at $Sc \approx 1$, and comparable Reynolds numbers made it possible to estimate the concentration spectra with enough spatial resolution directly, obviating the need for the compensation scheme employed here.

In the case of the present, liquid-phase data, we should entertain the possibility that the collapse of the spectra may be attributable to a fortuitous choice of the compensation pole. Some observations, however, are relevant here. First, the close agreement between the two spectra also holds in the $f\tau_\delta < 2$ frequency range, where the effects of compensation, even for the $x/d = 100$ data, are negligible. As we will see below, this will also be found to be the case at higher Reynolds numbers. Second, the value of the pole represents a single parameter. In contrast, the collapse of the spectra at the two axial locations, with substantially different degrees of compensation in each case, is over 5 orders of magnitude in the power spectra. Conversely, this collapse supports the validity of the single-pole model for the leading order behavior of the measurement transfer function.

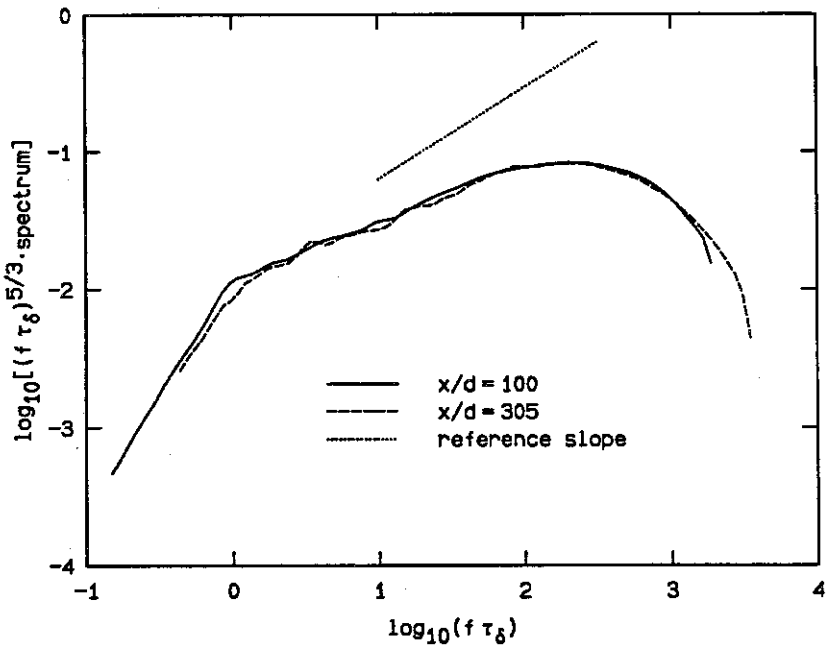


FIG. 6 Frequency-scaled concentration spectra. Solid line: $x/d = 100$ and $Re = 1.25 \times 10^4$. Dashed line: $x/d = 305$ and $Re = 1.2 \times 10^4$. Dotted line: reference line at a $^2/_3$ slope, corresponding to a $k^{-1}$ spectrum.

It is useful to plot the product of the concentration spectra with $f^{5/3}$, as is commonly done. A spectrum described by a $-^5/_3$ power-law yields a horizontal line over the $-^5/_3$ frequency range when plotted in this fashion. The product of the concentration spectra with $(f\tau_\delta)^{5/3}$, derived from the data at $x/d = 100$ and

$x/d = 305$, at $Re = 1.25 \times 10^4$ and $Re = 1.2 \times 10^4$, are plotted in Fig. 6 as the solid and dashed line curves, respectively. Also plotted, for reference, is a straight line with a slope (logarithmic derivative) of $^2/_3$, corresponding to the high-Schmidt number Batchelor $k^{-1}$ theoretical spectrum.[4]

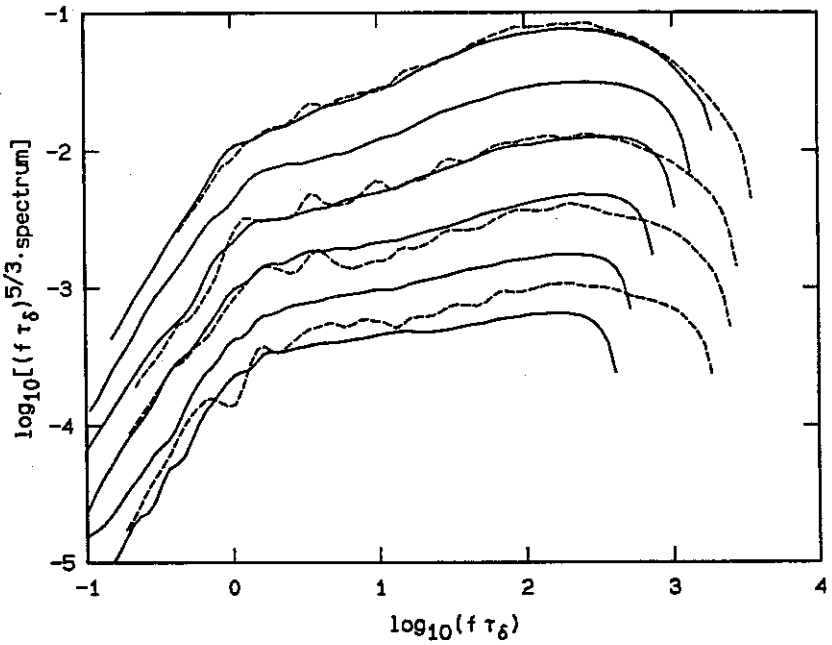


FIG. 7 Frequency-scaled concentration spectra. Solid lines: $x/d = 100$ data ($1.25 \leq Re \times 10^{-4} \leq 7.2$). Dashed lines: $x/d = 305$ data ($1.2 \leq Re \times 10^{-4} \leq 6.5$). Individual spectra are offset by $-2\log_{10}(Re/Re_0)$, $Re_0 = 1.2 \times 10^4$, for clarity.

The solid lines in Fig. 7 plot spectra derived from measurements at $x/d = 100$, for $Re \times 10^{-4} = 1.25$, 1.76, 2.55, 3.6, 5.1, and 7.2. The decrease in the scaled frequency resolved, in the $x/d = 100$ spectra, as the speed of the flow increased with increasing Reynolds number, is evident. The dashed lines plot spectra measured at $x/d = 305$, for $Re \times 10^{-4} = 1.2$, 2.4, 4.0, and 6.5. As can be seen, the highest frequency resolved in the $x/d = 305$ spectra is a much weaker function of Reynolds number, signal-to-noise ratio limitations being more serious than spatial resolution at this station. Individual spectra for both $x/d$ stations are plotted offset by $-2\log_{10}(Re/Re_0)$, with $Re_0 = 1.2 \times 10^4$, to aid in visualizing the evolution of trends with Reynolds number.

The longer characteristic local time scale at $x/d = 305$ did not allow as many large scale structures to be included in the record. As a consequence, the statistical convergence of the $x/d = 305$ spectra is not as good as for the $x/d = 100$ data. On the other hand, the higher relative spatial resolution at $x/d = 305$ allowed the spectrum to be estimated to a higher (scaled) frequency. That trade-off aside, the agreement between the (scaled) spectra at $x/d = 100$ and $x/d = 305$ holds for all the cases for which data were recorded at the same, or nearly the same, Reynolds number at the two stations.

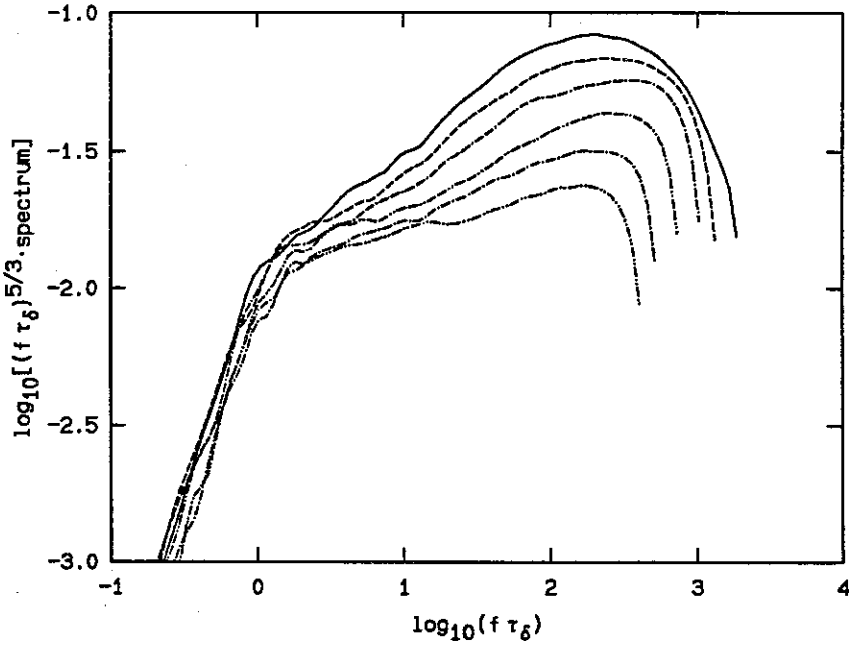


FIG. 8 Frequency-scaled concentration spectra derived from data at $x/d = 100$ and $1.25 \leq Re \times 10^{-4} \leq 7.2$ (no offsets).

Following the transition out of the large scale frequency regime ($f\tau_\delta \sim 1$), the spectra appear to be described by a power-law with an exponent that is increasing from, roughly, 1.2 to 1.5, in absolute value, with increasing Reynolds number (*cf.* Ref. 15, Fig. 5.2). This progression with Reynolds number is easier to discern in Fig. 8, which plots the concentration spectra at $x/d = 100$, for $Re \times 10^{-4} = 1.25$ (solid line), 1.76 (dashed line), 2.55 (dot–2-dash), 3.6 (2-dot–2-dash), 5.1 (dot–dash), and 7.2 (2-dot–dash), with no offsets. The extent of the power-law regime can be seen to increase slightly with increasing Reynolds number. A similarly

increasing spectral slope (in absolute value) with Reynolds number was also noted in measurements of gas-phase spectra,[23] for $Re \times 10^{-4} = 0.5$, 1.6, and 4.0.

As can be seen by sighting along the spectra in Fig. 8, the power-law region is followed by a different regime at higher frequencies yet. This regime does not support the Batchelor $k^{-1}$ prediction[4] that should apply for over a decade and a half in frequency in this case (recall that $Sc \approx 1.9 \times 10^3$ here). This can be seen in Fig. 6, which includes a dotted line with a reference slope of $^2/_3$, corresponding to a $k^{-1}$ spectrum. The spectra at increasing Reynolds number move even further from this slope, as can be seen by comparing the $Re = 1.2 \times 10^4$ spectrum with those at higher Reynolds numbers in Fig. 8. It should be noted that this conclusion extends to frequencies below $f\tau_\delta \simeq 2$, which are unaffected by resolution and compensation considerations.

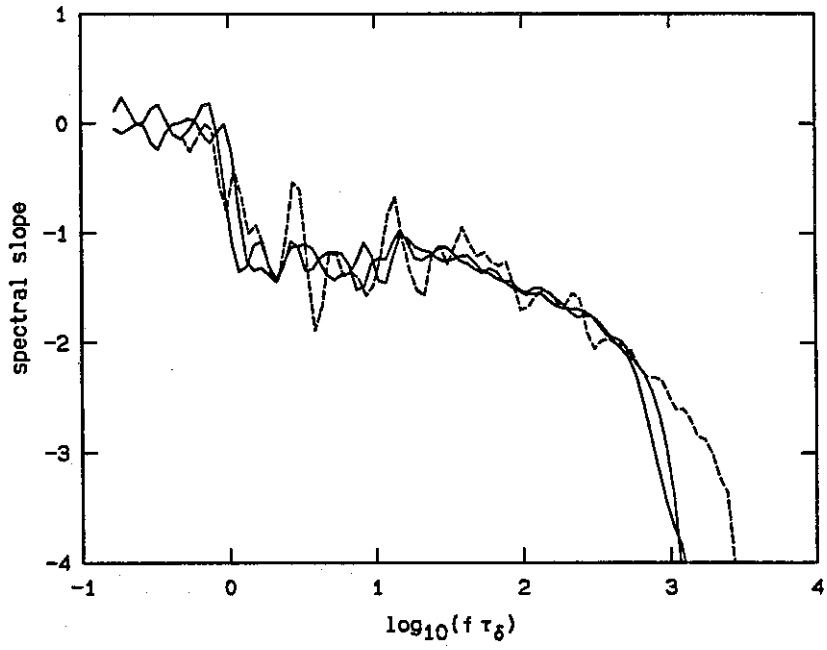


FIG. 9 Spectrum slope (logarithmic derivative). Solid lines: data at $x/d = 100$ and $Re = 1.25 \times 10^4$. Dashed line: $x/d = 305$, $Re = 1.2 \times 10^4$.

To facilitate the study of this higher frequency regime, we also computed the slope of the spectra (logarithmic derivative). A plot of spectrum slopes, for the lower Reynolds number data, appears in Fig. 9. These were derived from the two

$x/d = 100$, $Re = 1.25 \times 10^4$ spectra in Fig. 3 (solid lines) and the $x/d = 305$, $Re = 1.2 \times 10^4$ spectrum (dashed line). Their comparison helps assess issues of statistical convergence and confidence in this more delicate statistic, as well as the effects of spatial resolution and the applied compensation.

The plots in Fig. 9 suggest a frequency-dependence of the slope of the spectra that is close to a straight line, in these coordinates, for frequencies higher than $f\tau_\delta \simeq 1.2$, at this Reynolds number. This linear behavior extends for a decade and a half and into frequencies beyond which the data are limited by resolution and signal-to-noise considerations. The straight line appears to be a good representation for frequencies below $f\tau_\delta \approx 2$, for which the effects of compensation were negligible even for the $x/d = 100$ data (*cf.* Fig. 3). For frequencies above $f\tau_\delta \simeq 2$, the same straight line also describes the behavior for both the $x/d = 100$ and $x/d = 305$ data, which were affected by resolution (and compensation) to a different extent (*cf.* Figs. 3 and 5).

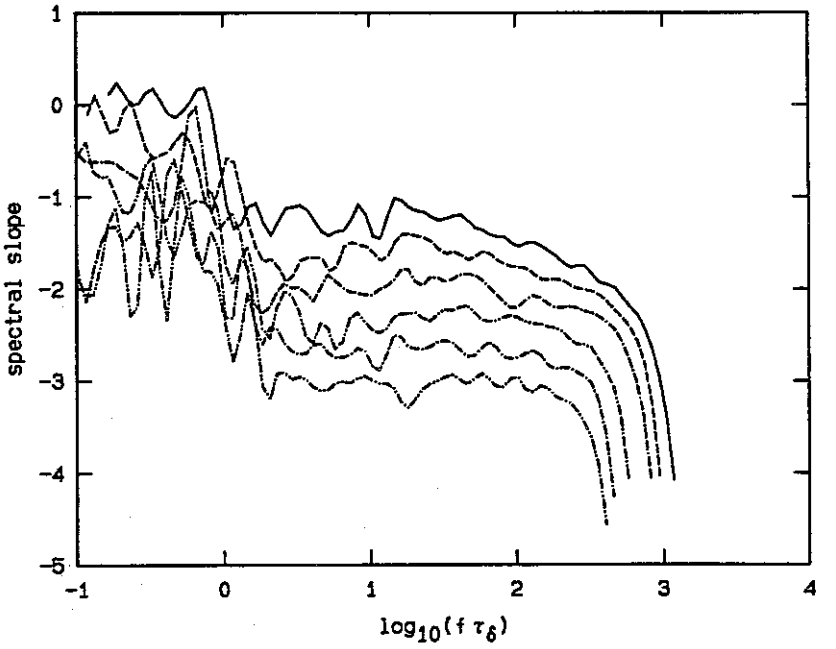


FIG. 10 Slope (logarithmic derivative) of spectra from data at $x/d = 100$ and $1.25 \leq Re \times 10^{-4} \leq 7.2$. Spectra offset as in Fig. 7. Line types as in Fig. 8.

A straight line for the logarithmic derivative of the spectrum corresponds to a spectrum that is parabolic in log-log coordinates, or log-normal in linear coordinates, *i.e.*,

$$S_c(f\tau_\delta) \propto \exp\left\{-\frac{1}{2}\left[a\ln(f\tau_\delta) + b\right]^2\right\} . \qquad (18)$$

This expression, rather than a $k^{-1}$ power law, seems to be the appropriate description of our jet fluid concentration spectra at high frequencies, over a range of frequencies at least as large as $\sqrt{Sc}$, *i.e.*, a decade and a half, in this case.

Figure 10 plots the local slope (logarithmic derivative) of the spectra in Fig. 8. The offset scheme employed in Fig. 7, and line-types employed in Fig. 8, were also used here. Straight lines can be seen to be a good representation for the spectrum slope at high frequencies with Reynolds number dependent values of the parameters $a$ and $b$ in Eq. 18. The end of the power-law regime and the beginning of the log-normal range can be seen to shift to higher frequencies with increasing Reynolds number. Our data admit a Kolmogorov scaling for the Reynolds number dependence of this transition frequency, *i.e.*, $Re^{3/4}$, but corresponding to the convection (passage frequency) of a physical scale roughly 80 times larger than the estimated Kolmogorov scale (computed using the estimated mean centerline energy dissipation[25] and the kinematic viscosity). This transition is not very well defined, however, and other Reynolds number scaling possibilities cannot be ruled out.

## 5. Conclusions

This work has investigated temporal scalar (jet fluid concentration) power spectra on the centerline of high Schmidt number turbulent jets, in the Reynolds number range $1.2 \leq Re \times 10^{-4} \leq 7.2$. Our spectra exhibit a power-law regime at frequencies above the local large scale passage frequency, with a Reynolds number dependent exponent increasing (in absolute value) from, roughly, $-1.2$ to $-1.5$ over the Reynolds number range investigated. This corroborates a similar finding for gas-phase jet fluid concentration spectra measured at comparable Reynolds numbers.[23] At higher frequencies, the spectra are well represented by a log-normal relation with Reynolds number dependent coefficients. While our data admit a Kolmogorov-like

scaling for the beginning of the log-normal region in the spectrum, *i.e.*, $\sim Re^{3/4}$, other possibilities cannot be ruled out.

We appreciate that our results are at odds with the classical picture of high Schmidt number scalar spectra. We do not find a $-5/3$ power-law regime, even though our measurements were conducted at Reynolds numbers where such behavior has previously been reported for high Schmidt number jet fluid scalar spectra.[26] Finally, despite adequate resolution and signal-to-noise ratio, our data do not support the Batchelor $k^{-1}$ power-law prediction.[4] Specifically, we found no constant $k^{-1}$ slope at high frequencies and a spectral slope that does not even locally attain a value of $-1$.

On the whole, our scalar spectra are rather similar to those derived by Gargett from ocean measurements.[11] In conjunction with her data and analysis, the current results raise further questions about the universal descriptions of scalar spectra, and their applicability to some of the canonical flows, such as turbulent jets.

## Acknowledgments

We would like to acknowledge contributions by Dan Lang and David Dowling to the experiments. This work was supported by AFOSR Grants No. 83-0213 and 88-0155, and GRI Contract No. 5087-260-1467.

## References

[1] Kolmogorov, A. N., "Local Structure of Turbulence in an Incompressible Viscous Fluid at Very High Reynolds Numbers," *Dokl. Akad. Nauk SSSR* **30**, 299 (1941).

[2] Corrsin, S., "On the spectrum of isotropic temperature fluctuations in isotropic turbulence," *J. Appl. Phys.* **22**, 469–473 (1951).

[3] Oboukhov, A. M., "Some specific features of atmospheric turbulence," *J. Fluid Mech.* **13**, 77–81 (1962).

[4] Batchelor, G. K., "Small-scale variation of convected quantities like temperature in turbulent fluid. Part 1. General discussion and the case of small conductivity," *J. Fluid Mech.* **5**, 113–133 (1959).

[5] Monin, A. S., and Yaglom, A. M., *Statistical Fluid Mechanics: Mechanics of Turbulence* **II** (Ed. J. Lumley, MIT Press, Cambridge, MA, 1975).

[6] Gibson, C. H., "Kolmogorov similarity hypotheses for scalar fields: sampling intermittent turbulent mixing in the ocean and galaxy," *Proc. Roy. Soc.* A **434**, 149–164 (1991).

[7] Chapman, D. R., "Computational Aerodynamics Development and Outlook," *AIAA J.* **17**(12), 1293-1313 (1979).

[8] Batchelor, G. K., Howells, I. D. , and Townsend, A. A., "Small-scale variation of convected quantities like temperature in turbulent fluid. Part 2. The case of large conductivity," *J. Fluid Mech.* **5**, 134-139 (1959).

[9] Gibson, C. H., and Schwarz, W. H., "The universal equilibrium spectra of turbulent velocity and scalar fields," *J. Fluid Mech.* **16**, 365–384 (1963).

[10] Grant, H. L., Hughes, B. A., Vogel, W. M., and Moilliet, A., "The spectrum of temperature fluctuations in turbulent flow," *J. Fluid Mech.* **34**, 423–442 (1968).

[11] Gargett, A. E., "Evolution of scalar spectra with the decay of turbulence in a stratified fluid," *J. Fluid Mech.* **159**, 379–407 (1985).

[12] Gibson, C. H., "Fossil turbulence and intermittency in sampling oceanic mixing processes," *J. Geophys. Res.* **92**, C5, 5383–5404 (1987).

[13] Komori, S., Kanzaki, T., Murakami, Y., and Ueda, H., "Simultaneous measurements of instantaneous concentrations of two species being mixed in a turbulent flow by using a combined laser-induced fluorescence and laser-scattering technique," *Phys. Fluids* A **1**(2), 349–352 (1989).

[14] Miller, P. L., and Dimotakis, P. E., "Reynolds number dependence of scalar fluctuations in a high Schmidt number turbulent jet," *Phys. Fluids A* **3**(5), 1156–1163 (1991).

[15] Miller, P. L., *Mixing in High Schmidt Number Turbulent Jets*, Ph.D. thesis, California Institute of Technology (1991).

[16] Dimotakis, P. E., and Miller, P. L., "Some consequences of the boundedness of scalar fluctuations," *Phys. Fluids A* **2**(11), 1919–1920 (1990).

[17] Miller, P. L., and Dimotakis, P. E., "Stochastic geometric properties of scalar interfaces in turbulent jets," *Phys. Fluids A* **3**(1), 168–177 (1991).

[18] Ware, B. R., Cyr, D., Gorti, S., and Lanni, F., "Electrophoretic and Frictional Properties of Particles in Complex Media Measured by Laser Light Scattering and Fluorescence Photobleaching Recovery," *Measurement of Suspended Particles by Quasi-Elastic Light Scattering* (Wiley, NY), 255–289 (1983).

[19] Blake, W. K., *Mechanics of Flow-Induced Vibration.* **II** (Academic Press, Orlando, FL, 1986).

[20] Young, F. R., *Cavitation* (McGraw-Hill, London, 1989).

[21] Dowling, D. R., Lang, D. B., and Dimotakis, P. E., "An Improved Laser-Rayleigh Scattering Photodetection System," *Exp. in Fluids* **7**(7), 435–440 (1989).

[22] Chen, C. J., and Rodi, W., *Vertical Turbulent Buoyant Jets. A Review of Experimental Data* (Pergammon Press, Oxford, 1980).

[23] Dowling, D. R., and Dimotakis, P. E., "Similarity of the concentration field of gas-phase turbulent jets," *J. Fluid Mech.* **218**, 109–141 (1990).

[24] Dowling, D. R., *Mixing in Gas Phase Turbulent Jets*, Ph.D. thesis, California Institute of Technology (1988).

[25] Friehe, C. A., Van Atta, C. W., and Gibson, C. H., "Jet turbulence: Dissipation rate measurements and correlations," AGARD *Turbulent Shear Flows* CP–93, 18.1–7 (1971).

[26] Becker, H. A., Hottel, H. C., and Williams, G. C., "The Nozzle-Fluid Concentration Field of the Round Turbulent, Free Jet," *J. Fluid Mech.* **30**(2), 285–303 (1967).